Dynamical bar-mode instability in rotating and magnetized relativistic stars

Luca Franci,[1] Roberto De Pietri,[1] Kyriaki Dionysopoulou,[2] and Luciano Rezzolla[2,3]

[1]*Università di Parma and INFN gruppo collegato di Parma, Italy*
[2]*Max-Planck-Institut für Gravitationsphysik, Albert-Einstein-Institut, Golm, Germany*
[3]*Institut für Theoretische Physik, Frankfurt am Main, Germany*

(Dated: January 11, 2014)

We present three-dimensional simulations of the dynamical bar-mode instability in magnetized and differentially rotating stars in full general relativity. Our focus is on the effects that magnetic fields have on the dynamics and the onset of the instability. In particular, we perform ideal-magnetohydrodynamics simulations of neutron stars that are known to be either stable or unstable against the purely hydrodynamical instability, but to which a poloidal magnetic field in the range of 10^{14}–10^{16} G is superimposed initially. As expected, the differential rotation is responsible for the shearing of the poloidal field and the consequent linear growth in time of the toroidal magnetic field. The latter rapidly exceeds in strength the original poloidal one, leading to a magnetic-field amplification in the the stars. Weak initial magnetic fields, i.e., $\lesssim 10^{15}$ G, have negligible effects on the development of the dynamical bar-mode instability, simply braking the stellar configuration via magnetic-field shearing, and over a timescale for which we derived a simple algebraic expression. On the other hand, strong magnetic fields, i.e., $\gtrsim 10^{16}$ G, can suppress the instability completely, with the precise threshold being dependent also on the amount of rotation. As a result, it is unlikely that very highly magnetized neutron stars can be considered as sources of gravitational waves via the dynamical bar-mode instability.

PACS numbers: 04.25.Dm, 04.40.Dg, 95.30.Lz, 97.60.Jd

I. INTRODUCTION

Main-sequence stars with masses greater than about $8\,M_\odot$ follow two evolutionary paths; either they form a degenerate core of O/Ne/Mg, or a degenerate Fe core, which, after undergoing a Type II supernova core collapse, forms a proto-neutron star [1, 2]. Neutron stars (NSs) are also expected to form through the accretion-induced collapse of a white dwarf [3, 4]. At birth, NSs are rapidly and differentially rotating, which makes them subject to various types of instabilities. Among these, the dynamical bar-mode instability and the shear-instability are particularly interesting because of their potential role as sources of gravitational waves (GWs).

Indeed, a newly born NS may develop a dynamical bar-mode instability when the rotation parameter $\beta := T/|W|$, with T the rotational kinetic energy and W the gravitational binding energy, exceeds a critical value β_c (see, for instance, [5, 6] for some reviews). Under these conditions, the rapidly rotating NS can become severely deformed, leading to a strong emission of GWs in the kHz range. Analytic investigations of the conditions under which these dynamical instabilities develop in self-gravitating rotating stars can be found in [7, 8], but these are inevitably restricted to Newtonian gravity or to simple shell models. To improve our understanding of these instabilities also in the nonlinear regimes, and to be able to extract useful physical information from the potential GW emission, it is clear that a general-relativistic numerical modeling is necessary. This has been the focus of a number of recent works, e.g., [9–12], which have provided important clues about the threshold for the instability and its survival under realistic conditions. As an example, for a polytropic relativistic star with polytropic index $\Gamma = 2$, the calculations reported in [10] revealed that the critical value is $\beta_c \sim 0.254$, and that a simple dependence on the stellar compactness can be used to track this threshold from the Newtonian limit over to the fully relativistic one [11]. Furthermore, numerical simulations have also revealed that the instability is in general short-lived and that the bar-deformation is suppressed over a timescale of a few revolutions (this was first pointed out in Ref. [10] and later confirmed in Ref. [13], where it was interpreted as due to a Faraday resonance).

One aspect of the bar-mode instability that so far has not received sufficient attention is about the occurrence of the instability in magnetized stars. This is not an academic question since NSs at birth are expected to be quite generically magnetized, with magnetic fields that have strengths up to $\simeq 10^{12}$ G in ordinary NSs and reaching strengths in excess of 10^{15} G in magnetars, if instabilities or dynamos have taken place in the proto-neutron star phase [14, 15].

Magnetic fields of this strength can affect both the structure and the evolution of NSs [16–19], and it is natural to expect that they will influence also the development of the instability when compared to the purely hydrodynamical case. A first dynamical study in this direction has been carried out recently in Ref. [20], where the development of the dynamical bar-mode instability has been studied for differentially rotating magnetized stars in Newtonian gravity and in the ideal-magnetohydrodynamics (MHD) limit (i.e., with a plasma having infinite conductivity). Not surprisingly, this study found that magnetic fields do have an effect on the development of the instability, but that this is the case only for very strong magnetic fields. We here consider the same problem, but extend the analysis to a fully general-relativistic framework, assessing the impact that the results have on high-energy astrophysics and GW astronomy.

Our investigation of the dynamics of highly-magnetized and rapidly rotating NSs is also part of a wider study of this type of objects to explain the phenomenology associated with short gamma-ray bursts. These catastrophic phenomena, in fact, are normally thought to be related to the merger of a

binary system of NSs [21–24], which could then lead to the formation of a long-lived hypermassive NS (HMNS) [25–28]. If highly magnetized, the HMNS could then also lead to an intense electromagnetic emission [29, 30]. This scenario has recently been considered in Refs. [31, 32], where numerical simulations of an axisymmetric differentially rotating HMNS were carried out. The HMNS had initially a purely poloidal magnetic field, which eventually led to a magnetically driven outflow along the rotation axis.

A similar setup has also been considered in a number of works, either in two-dimensional (2D) [33] or in three-dimensional (3D) simulations [34], with the goal of determining whether or not the conditions typical of a HMNS can lead to the development of the magnetorotational (MRI) instability [35]. Although this type of simulations in 3D still stretches the computational resources presently available, the very high resolutions employed in Ref. [34], and the careful analysis of the results, provided the first convincing evidence that the MRI can develop from 3D configurations. This has of course important consequences on much of the phenomenology associated with HMNSs, as it shows that very strong magnetic fields, up to equipartition, will be produced in the HMNS if this survives long enough for the MRI to develop.

In the simulations reported here we necessarily adopt much coarser resolutions and hence we will not be able to concentrate our attention on the development of the MRI. Rather, we will here extend our previous work on the dynamical bar-mode instability [10, 11, 36] also to the case of magnetized stars, determining when and how magnetic fields can limit the development of the dynamical bar-mode instability. Our initial models correspond to stationary equilibrium configurations of axisymmetric and rapidly rotating relativistic stars. More precisely, our initial models are described by a polytropic EOS with adiabatic index $\Gamma = 2$ and are members of a sequence with a constant rest-mass of $M \simeq 1.5\ M_\odot$ and a constant amount of differential rotation.

Interpreting the results of our simulations can be rather straightforward. Because we work in the ideal-MHD limit, the magnetic field lines are "frozen" in the fluid and follow its dynamics (see [37] for a recent extension of the code to resistive regime). As a consequence, differential rotation drives the initial purely poloidal magnetic field into rotation, winding it up and generating a toroidal component. At early times, the toroidal magnetic field grows linearly with time, tapping the NS's rotational energy. At later times, the growth starts deviating from the linear behavior and the magnetic tension produced by the very large magnetic-field winding, alters the angular velocity profile of the star. Depending on the models adopted and the initial magnetic field strength, the magnetic winding could become the most efficient mechanisms for redistributing angular momentum, with the MRI being the dominant one when the Alfvén timescale becomes comparable to the magnetic winding timescale.

Overall, we find that if the initial magnetic fields are $\lesssim 10^{15}$ G, then they have a negligible effect on the occurrence of the dynamical bar-mode instability, which develops in close analogy with the purely hydrodynamical case. On the other hand, if the initial magnetic fields are $\gtrsim 10^{16}$ G, they can suppress the instability completely. Note that the precise threshold marking the stability region depends not only on the strength of the magnetic field, but also on the amount of rotation. We trace this threshold by performing a number of simulations of a number of sequences having the same parameter β but different magnetizations. An important consequence of our results is that because the instability is suppressed in strongly magnetized NSs, these can no longer be considered as potential sources of GWs, at least via the dynamical bar-mode instability.

The organization of the paper is as follows. In Sect. II we describe the numerical methods and the setup employed in our simulations, as well as the full set of equations we solve. In Sect. III we mention briefly the main properties of the stellar models adopted as initial data, together with the simplifications and assumptions we make. In Sect. IV we examine in great detail the effects of the presence of an initial poloidal magnetic field on differentially rotating stars covering a wide range in the parameter space. We further discuss the qualitative and quantitative features of the evolution of models with the same total rest mass but different rest-mass density and angular momentum profiles that are known to be unstable to the purely hydrodynamic bar-mode instability. Finally, we investigate whether magnetic fields affect the stellar evolution even when the bar-mode instability does not develop. Our conclusions are drawn in Sect. V and two appendices discuss the influence of symmetries on the development of the instability and the convergence of our results. Unless stated differently, we adopt geometrized units in which $c = 1$, $G = 1$, $M_\odot = 1$.

II. MATHEMATICAL AND NUMERICAL SETUP

The simulations have been carried out using the general-relativistic ideal-MHD (GRMHD) code `WhiskyMHD` [24, 38, 39]. The code provides a 3D numerical solution of the full set of the GRMHD equations in flux-conservative form on a dynamical background in Cartesian coordinates. It is based on the same high-resolution shock-capturing (HRSC) techniques on domains with adaptive mesh refinements (AMR) [40, 41]) as discussed in [42]. The reconstruction method adopted is the one discussed in the piecewise parabolic (PPM) [43], while the Harten-Lax-van Leer-Einfeldt (HLLE) approximate Riemann solver [44] has been employed in order to compute the fluxes. The divergence of the magnetic field is enforced to stay within machine precision by employing the flux-CD approach as implemented in [39], but with the difference that we adopt as evolution variable the vector potential instead of the magnetic field. This method ensures the divergence-free character of the magnetic field since the magnetic field is computed as the curl of the evolved vector potential using the same finite-differencing operators as the ones for computing the divergence of the magnetic field.

Because of the gauge invariance of Maxwell equations, a choice needs to be made and we have opted for the simplest one, namely, the algebraic Maxwell gauge. This choice can introduce some spurious oscillations close to the AMR boundaries in highly dynamical simulations, but this has not been

the case for the simulations reported here. On the other hand, it has allowed us to keep the divergence of the magnetic field essentially nearly at machine precision. A more advanced prescription has been also introduced recently in Ref. [45]; this approach requires a certain amount of tuning for optimal performance and will be considered in future works. Additional information on the code can also be found in Refs. [38, 39].

Furthermore, to remove spurious post-shock oscillations in the magnetic field we add a fifth-order Kreiss-Oliger type of dissipation [46] to the vector potential evolution equation with a dissipation parameter of 0.1. Finally, the evolution of the gravitational fields is obtained through the `CCATIE` code, which provides the solution of the conformal traceless formulation of the Einstein equations [47]. The time integration of the evolution equations is achieved through a third-order accurate Runge-Kutta scheme. Essentially all of the simulations presented in this paper use a 3D Cartesian grid with four refinement levels and with outer boundaries located at a distance ~ 150 km from the center of the grid. The finest resolution is $\Delta x \simeq 0.550$ km (between 40 and 60 points across the stellar radius, depending on the model) and the coarsest extends up to about ~ 150 km, namely more than five times the stellar radius. Unless stated differently, all of the simulations discussed hereafter have been performed imposing a bitant symmetry, i.e., a reflection symmetry across the $z = 0$ plane.

For convenience we report here the full set of the evolution equations we solve numerically which consists in the coupled systems of Einstein and MHD equations, i.e.,

$$R_{\mu\nu} - \frac{1}{2} g_{\mu\nu} R = 8\pi T_{\mu\nu} \,, \tag{2.1}$$

$$\nabla_\mu T^{\mu\nu} = 0 \,, \tag{2.2}$$

$$\nabla_\mu (\rho u^\mu) = 0 \,, \tag{2.3}$$

$$\nabla^\star_\mu F^{\mu\nu} = 0 \,, \tag{2.4}$$

$$\nabla_\mu F^{\mu\nu} = 4\pi \mathcal{J}^\nu \,, \tag{2.5}$$

where $R_{\mu\nu}, g_{\mu\nu}$ and R are the Ricci tensor, the metric tensor and the Ricci scalar, respectively. On the electromagnetic side, $F_{\mu\nu}$ is the Maxwell tensor, dual of the Faraday tensor ${}^*F_{\mu\nu}$, $\mathcal{J}^\mu$ is the current four-vector, and on the matter side ρ is the rest-mass density, u^μ is the 4-velocity of the fluid satisfying the normalization condition $u_\mu u^\mu = -1$. The total energy-momentum tensor $T^{\mu\nu}$ is the linear combination of the contributions coming from a perfect fluid, i.e., $T^{\mu\nu}_{\rm fl}$, and from the electromagnetic fields, i.e., $T^{\mu\nu}_{\rm em}$

$$T^{\mu\nu} = T^{\mu\nu}_{\rm em} + T^{\mu\nu}_{\rm fl} \,.$$

where

$$T^{\mu\nu}_{\rm fluid} := \rho h u^\mu u^\nu + p g^{\mu\nu} \,, \tag{2.6}$$

$$\begin{aligned} T^{\mu\nu}_{\rm em} &:= F^{\mu\sigma} F^\nu{}_\sigma - \frac{1}{4} g^{\mu\nu} F_{\alpha\beta} F^{\alpha\beta} \\ &= \left(u^\mu u^\nu + \frac{1}{2} g^{\mu\nu} \right) b^2 - b^\mu b^\nu \,, \end{aligned} \tag{2.7}$$

In the expressions above we recall that $h = 1 + \epsilon + p/\rho$ is the specific enthalpy, ϵ the specific internal energy. Hence, the energy density in the rest-frame of the fluid is just $e = \rho(1+\epsilon)$. At the same time, the four-vector b^μ represents the magnetic field as measured in the comoving frame, so that the Maxwell and Faraday tensors are expressed as (see [38, 39] for details)

$$F^{\mu\nu} = \epsilon^{\mu\nu\alpha\beta} u_\alpha b_\beta = n^\mu E^\nu - n^\nu E^\mu + \epsilon^{\mu\nu\alpha\beta} B_\alpha n_\beta \,, \tag{2.8}$$

$${}^*F^{\mu\nu} = b^\mu u^\nu - b^\nu u^\mu = n^\mu B^\nu - n^\nu B^\mu - \epsilon^{\mu\nu\alpha\beta} E_\alpha n_\beta \,, \tag{2.9}$$

where the second equalities introduce the electric and magnetic fields measured by an observer moving along a normal direction n^ν. We further note that the $\sqrt{4pi}$ terms appearing in Eqs. (2.4),(2.5) are absorbed in the definition of the magnetic field.

In the interest of compactness, we will not discuss here the detailed formulation of the Eqs. (2.1)–(2.3) we use in the numerical solution and refer the interested reader to the following works where these aspects are discussed in detail: Ref. [47] for the formulation of the Einstein equations and the gauge conditions used, Refs. [38, 39] for the formulation of the MHD equations and the strategy for enforcing a zero divergence of the magnetic field, Refs. [27, 48] for the computational infrastructure and the numerical methods used. What is however important to remark here is that we employ an "ideal-fluid" (or Gamma-law) equation of state (EOS) [48]

$$p = \rho\, \epsilon (\Gamma - 1) \,, \tag{2.10}$$

where Γ is the adiabatic exponent, which we set to be $\Gamma = 2$. More realistic EOS could have been used, as done for instance in Ref. [49], and this will indeed be the focus of future work. At this stage, however, and because this is the first study of this type, the simpler analytic EOS (2.10) is sufficient to collect the first qualitative aspects of the development of the instability.

III. INITIAL DATA AND DIAGNOSTICS

The initial data of our simulations are computed as stationary equilibrium solutions of axisymmetric and rapidly rotating relativistic stars in polar coordinates and without magnetic fields [50]. In generating these equilibrium models we adopt a "polytropic" EOS [48], $p = K\rho^\Gamma$, with $K = 100$ and $\Gamma = 2$, and assume the line element for an axisymmetric and stationary relativistic spacetime to have the form

$$\begin{aligned} ds^2 = &-e^{\mu+\nu} dt^2 + e^{\mu-\nu} r^2 \sin^2\theta (d\phi - \omega dt)^2 \\ &+ e^{2\xi} (dr^2 + r^2 d\theta^2) \,, \end{aligned} \tag{3.1}$$

where μ, ν, ω and ξ are space-dependent metric functions. To reach the large angular momentum needed to trigger the dynamical bar-mode instability, a considerable amount of differential rotation needs to be introduced and we do so following the traditional constant specific angular momentum law

Model	ρ_c (10^{-4})	r_p/r_e	A_b	R_e [km]	M_0 $[M_\odot]$	M $[M_\odot]$	M/R_e	J	J/M^2	Ω_c [rad/s]	Ω_e [rad/s]	T (10^{-2})	W (10^{-2})	β	$\beta_{\rm mag}$ (10^{-6})
U13	0.599	0.200	1.85×10^6	35.9	1.505	1.462	0.0601	3.747	1.753	3647	1607	2.183	7.764	0.2812	5.3
U11	1.092	0.250	1.46×10^6	34.4	1.507	1.460	0.0627	3.541	1.661	3997	1747	2.284	8.327	0.2743	4.7
U3	1.672	0.294	8.74×10^5	32.4	1.506	1.456	0.0664	3.261	1.538	4434	1916	2.352	9.061	0.2596	3.5
S1	1.860	0.307	6.94×10^5	31.6	1.512	1.460	0.0682	3.191	1.497	4593	1976	2.384	9.388	0.2540	3.0
S6	2.261	0.336	4.50×10^5	30.0	1.505	1.449	0.0713	2.965	1.412	4901	2093	2.369	9.859	0.2403	2.3
S7	2.754	0.370	2.01×10^5	28.1	1.506	1.447	0.0760	2.741	1.309	5284	2234	2.360	10.56	0.2234	1.0
S8	3.815	0.443	5.96×10^4	26.7	1.506	1.439	0.0862	2.322	1.121	5995	2482	2.255	11.96	0.1886	0.4

TABLE I. Main properties of the stellar models evolved in the simulations. In the first column we report the model name, while in the next three the parameters we used to generate the initial models, namely the central rest-mass density ρ_c, the ratio between the polar and the equatorial coordinate radii r_p/r_e and the parameter A_b of Eq. (3.10) that would generate a magnetic field whose initial maximum value in the (x, y) plane is 1×10^{15} G. In the remaining columns we report, from left to right, the proper equatorial radius R_e, the rest mass M_0, the gravitational mass M, the compactness M/R_e, the total angular momentum J, J/M^2, the angular velocities at the axis $\Omega_c = \Omega(r = 0)$ and at the equator $\Omega_e = \Omega(r = R_e)$, the rotational kinetic energy T and the gravitational binding energy W, their ratio $\beta = T/|W|$ (instability parameter) and finally the ratio between the total magnetic energy and the sum of the rotational energy and the gravitational binding energy ($\beta_{\rm mag} = E_{\rm mag}/(T + |W|)$). Unless explicitly stated, all these quantities are expressed in geometrized units in which $G = c = M_\odot = 1$.

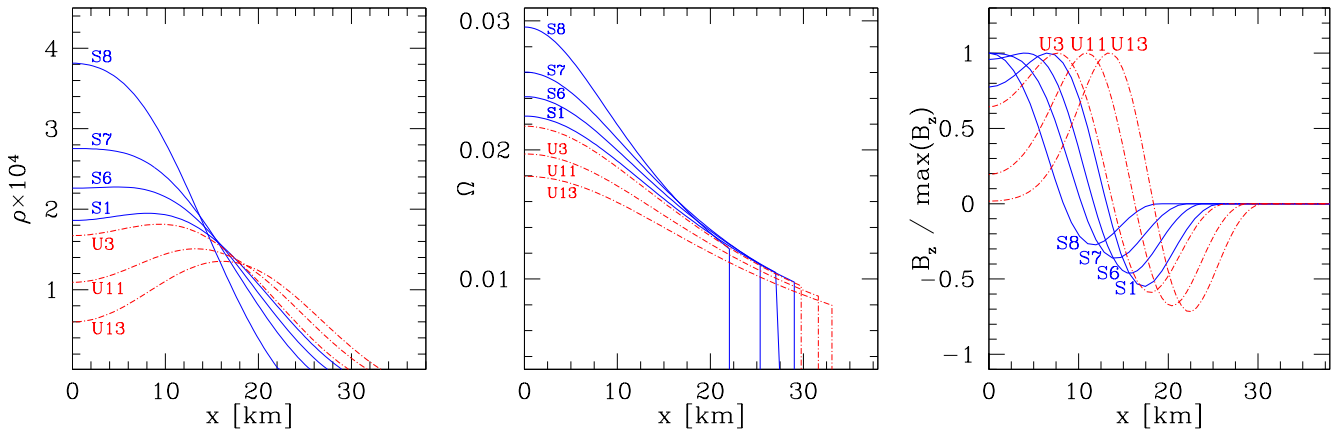

FIG. 1. Initial profiles of the rest-mass density ρ (left panel), the angular velocity Ω (center panel) and of the z-component of the magnetic field (right panel) for models S8, S7, S6, S1, U3, U11 and U13. The profiles of the stable models are here drawn with blue solid lines, while those for the unstable models with red dot-dashed lines.

("j-constant") of differential rotation, in which the angular velocity distribution takes the form [51, 52]

$$\Omega_c - \Omega = \frac{1}{\hat{A}^2 R_e^2}\left[\frac{(\Omega-\omega)r^2\sin^2\theta e^{-2\nu}}{1-(\Omega-\omega)^2 r^2\sin^2\theta e^{-2\nu}}\right], \quad (3.2)$$

where R_e is the coordinate equatorial stellar radius and the coefficient $\hat{A}$ is a measure of the degree of differential rotation, which we set to $\hat{A} = 1$ in analogy with other works in the literature. Once imported onto the Cartesian grid and throughout the evolution, we compute the angular velocity Ω (and the period P) on the (x, y) plane as

$$\Omega := \frac{u^\phi}{u^0} = \frac{u^y\cos\phi - u^x\sin\phi}{u^0\sqrt{x^2+y^2}}, \qquad P = \frac{2\pi}{\Omega}. \quad (3.3)$$

Other characteristic quantities of the system, such as the baryon mass M_0, the gravitational mass M, the angular momentum J, the rotational kinetic energy T, and the gravitational binding energy W are calculated as in [53]

$$M := \int d^3x\,\alpha\sqrt{\gamma}\left[-2(T_{\rm fl})^0{}_0 + (T_{\rm fl})^\mu{}_\mu\right], \quad (3.4)$$

$$M_0 := \int d^3x\,\sqrt{\gamma}D, \quad (3.5)$$

$$E_{\rm int} := \int d^3x\,\sqrt{\gamma}D\epsilon, \quad (3.6)$$

$$J := \int d^3x\,\alpha\sqrt{\gamma}(T_{\rm fl})^0{}_\phi, \quad (3.7)$$

$$T := \frac{1}{2}\int d^3x\,\alpha\sqrt{\gamma}\Omega(T_{\rm fl})^0{}_\phi, \quad (3.8)$$

$$W := T + E_{\rm int} + M_0 - M, \quad (3.9)$$

where ϵ is the specific internal energy, D is the conserved rest-mass density, γ is the determinant of the three-metric and $(T_{\rm fl})^\mu{}_\nu$ corresponds to the fluid contributions to the stress-energy tensor. A couple of important caveats need to be made about the definitions above. First, we note that we have

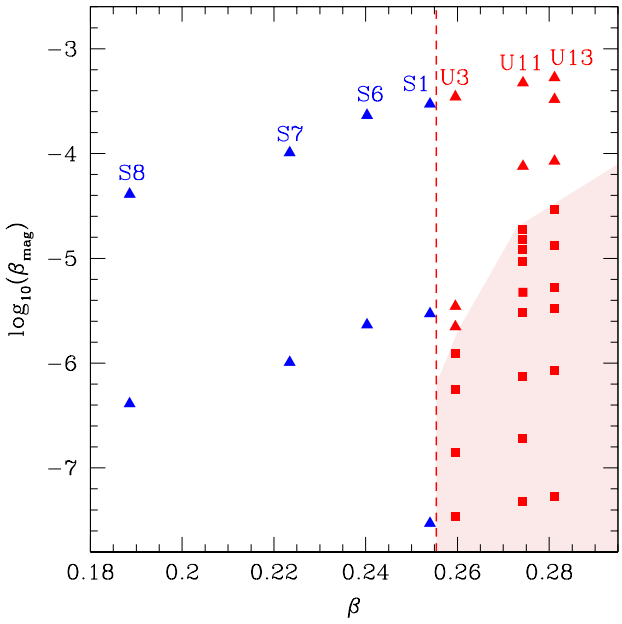

FIG. 2. Representation of the initial models in a $(\beta, \beta_{\rm mag})$ plane. Blue and red symbols mark models that are respectively bar-mode stable and bar-mode unstable at zero magnetizations, while the vertical red dashed line marks the stability threshold for zero magnetic fields. The red-shaded area collects as a function of their magnetization models that the evolutions reveal to be bar-mode unstable; hence, red squares refer to initial models that develop a bar-mode instability, while red triangles refer to potentially bar-unstable models that are stabilized by the strong magnetic fields.

defined the gravitational mass and angular momentum taking into account only the fluid part of the energy-momentum tensor and thus neglecting the electromagnetic contributions. This is strictly speaking incorrect, but tolerable given that the relative electromagnetic contributions to the mass and angular momentum are $\lesssim 10^{-5}$. Second, the definitions above for J, T, W and β are meaningful only in the case of stationary axisymmetric configurations and should therefore be treated with care once the rotational symmetry is lost.

The main properties of all the stellar models we have used as initial data are reported in Table I, where we have introduced part of our notation to distinguish the different models. In particular models indicated as `U*` and as `S*` refer to NSs that are unstable and stable to the purely dynamical bar-mode instability, respectively (this result was determined in Refs. [10, 11]). Figure 1 shows the initial profiles of the rest-mass density ρ (left panel), of the rotational angular velocity Ω (central panel), and of the z-component of the magnetic field (right panel) for all the models we have evolved. The profiles for the models that are unstable in the unmagnetized case are drawn with blue solid lines, while we use red dot-dashed lines for stable models. Note that the position of the maximum of the rest-mass density coincides with the center of the star only for models with low β; for those with a larger β, the maximum of the rest-mass density resides, instead, on a circle on the equatorial plane.

All the equilibrium models are members of a sequence having a constant rest-mass $M_0 \simeq 1.5\, M_\odot$ and are stable to gravitational collapse on the basis of the results of [54]. An initial poloidal magnetic field is added as a perturbation to the initial equilibrium models by introducing a purely toroidal vector potential A_ϕ given by

$$A_\phi = A_b \left(\max(p - p_{\rm cut}, 0)\right)^2 , \tag{3.10}$$

where $p_{\rm cut}$ is 4 % of the maximum pressure, while A_b is chosen in a way to have the chosen value for the maximum of the initial magnetic field B. The Hamiltonian and momentum constraint equations are not solved after superimposing the magnetic field, but we have verified that for the magnetic-field strength considered here, this perturbation introduces only negligible additional violations of the constraints.

The strength of the initial magnetic field can be characterized by the value of the ratio between the total magnetic energy

$$E_{\rm mag} := \int d^3x\, \alpha^2 \sqrt{\gamma}\, T^{00}_{\rm em} , \tag{3.11}$$

and the sum of the rotational kinetic energy T and of the gravitational binding energy W, which we indicate as $\beta_{\rm mag} := E_{\rm mag}/(T + |W|)$, in analogy with the instability parameter $\beta := T/|W|$. This parameter should not be confused with what is usually defined as the β parameter of a plasma, i.e., the ratio of the fluid pressure to the magnetic pressure.

In Table I we also report the values of the coefficient A_b [see Eq. (3.10)] and the parameter $\beta_{\rm mag}$ corresponding to an initial poloidal magnetic field strength equal to 10^{15} G. All the initial models are also reported in Fig. 2 according to the values of their parameters β and $\beta_{\rm mag}$. The models that are known to be stable against the bar-mode instability in the unmagnetized case are here drawn in blue (`S1`, `S6`, `S7` and `S8`), while the unstable ones are drawn in red (`U3`, `U11` and `U13`). The different symbols used in this figure will be further discussed in Sect. IV when illustrating the results of our work; it is sufficient to say for now that squares and triangles refer to unstable models with unmodified and modified growth times, respectively. Hereafter we will also extend our notation and denote a particular magnetized model by marking it by the maximum initial value of the z-component of the magnetic field on the (x, y) plane, i.e., $B^z_{\rm max}|_{t,z=0}$, expressed in Gauss. As an example, the bar-mode unstable model with initial $B^z_{\rm max}|_{t,z=0} = 1.0 \times 10^{15}$ G will be indicated as `U11-1.0e15`.

In order to analyze better the effects of magnetic fields on the dynamics of the bar-mode instability, we have introduced additional diagnostic variables to quantify and describe the evolution of the magnetic field itself. For axisymmetric configurations one usually decomposes the magnetic field in toroidal and poloidal components, studying their dynamics separately. When axisymmetry is lost, however, this nice decomposition is no longer available. Nevertheless, there exists a decomposition that can be defined even if axisymmetry is not preserved, which is reduced to the usual poloidal-toroidal one in the axisymmetric stationary case. The main idea of this decomposition is to separate the magnetic field in a component in the direction of the fluid motion and hence parallel to

the fluid three-velocity and in a component that is orthogonal to it. We therefore split the magnetic field measured by an Eulerian observer as

$$B^i = B_\parallel \frac{v^i}{\sqrt{\gamma_{ij} v^i v^j}} + B^i_\perp \,, \tag{3.12}$$

where we define the "perpendicular" part of the magnetic field from the condition $B^i_\perp v_i = 0$, while the "parallel" part is a scalar and is trivially defined as $B_\parallel := B^j v_j/(v^i v_i)^{1/2}$. Initially, when the flow is essentially azimuthal, $B^i_\perp$ corresponds to the poloidal component of the magnetic field, while $B_\parallel v^i/(v^j v_j)^{1/2}$ to the toroidal component. Hereafter we will refer loosely to these as the "poloidal" and "toroidal" components, respectively.

Within this decomposition, we can then define the electromagnetic energy contributions associated to the "toroidal" and "poloidal" magnetic-field components as

$$E^{\rm tor}_{\rm mag} := \int d^3x \, \sqrt{\gamma} \, \frac{1}{2} B_\parallel B_\parallel \,, \tag{3.13}$$

$$E^{\rm pol}_{\rm mag} := \int d^3x \, \sqrt{\gamma} \, \frac{1}{2} \gamma_{ij} B^i_\perp B^j_\perp (1 + \gamma_{rs} v^r v^s) \,. \tag{3.14}$$

Note that the total electromagnetic energy satisfies the condition $E_{\rm mag} = E^{\rm tor}_{\rm mag} + E^{\rm pol}_{\rm mag}$, since the electric field E^i provides a contribution to the energy, $E^i E_i = (v^i v_i)(B^i B_i - B^2_\parallel)$, that is already included in the definitions (3.13) and (3.14). Another important set of diagnostic quantities focuses instead on the detection of a bar deformation, which can be conveniently quantified in terms of the distortion parameters [55]

$$\eta_+ := \frac{I^{xx} - I^{yy}}{I^{xx} + I^{yy}} \,, \tag{3.15}$$

$$\eta_\times := \frac{2\, I^{xy}}{I^{xx} + I^{yy}} \,, \tag{3.16}$$

$$\eta := \sqrt{\eta_+^2 + \eta_\times^2} \,, \tag{3.17}$$

where the quadrupole moment of the matter distribution can be computed in terms of the conserved density D as in [10, 56]

$$I^{jk} = \int d^3x \, \sqrt{\gamma} D \, x^j x^k \,. \tag{3.18}$$

Note that all quantities in Eqs. (3.15)–(3.17) are expressed in terms of the coordinate time t and do not represent therefore invariant measurements at spatial infinity. However, for the simulations reported here, the length-scale of variation of the lapse function at any given time is always larger than twice the stellar radius at that time, ensuring that the events on the same time-slice are also close in proper time.

In addition, η_+ can be conveniently used to quantify both the growth time $\tau_{\rm bar}$ of the instability and the oscillation frequency $f_{\rm bar}$ of the unstable bar once the instability is fully developed. In practice, we obtain a measurement of $\tau_{\rm bar}$ and $f_{\rm bar}$ by performing a nonlinear least-square fit of the computed distortion $\eta_+(t)$ with the trial function

$$\eta_+(t) = \eta_0 \, e^{t/\tau_{\rm B}} \cos(2\pi \, f_{\rm B} \, t + \phi_0) \,. \tag{3.19}$$

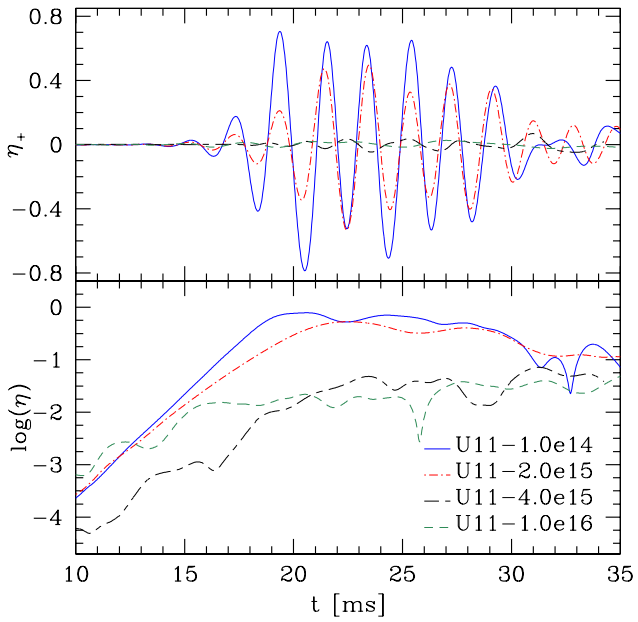

FIG. 3. Evolution of the distortion parameters η_+ and η for model `U11` with four different values of the initial poloidal magnetic field: $B^z_{\rm max}|_{t,z=0} = 1.0\times10^{14}$, 2.0×10^{15}, 4.0×10^{15}, and 1.0×10^{16} G.

IV. RESULTS

A. Effects of the magnetic field on unstable models

We start by discussing in detail the results relative to model `U11` when evolved for different values of the initial poloidal magnetic field. The dynamics of this unstable model are very clear and allow us to show a full qualitative and quantitative picture of what happens as the bar-mode instability develops. We will therefore focus our attention on models `U11-1.0e14`, `U11-2.0e15`, `U11-4.0e15` and `U11-1.0e16`, which, as discussed before, have initial poloidal magnetic field such that $B^z_{\rm max}|_{t,z=0}$ is equal to 1.0×10^{14}, 2.0×10^{15}, 4×10^{15} and 1.0×10^{16} G, respectively.

In Fig. 3 we show the evolution of the distortion parameters η_+ (top panel) and η (bottom panel) for these models. In the least magnetized model (i.e., `U11-1.0e14`), η_+ starts oscillating after about 10 ms of evolution with an amplitude that almost reaches unity, and it keeps oscillating for about 20 ms. At the same time, η undergoes an exponential growth, increasing its value by about three orders of magnitude until it reaches a saturation level, which persists for about 10 ms and then decays. This is exactly the behavior we expect from a stellar model which is unstable against the dynamical bar-mode instability, as model `U11` is known to be in the unmagnetized case (cf., Refs. [10, 56]).

However, when the initial poloidal magnetic field is two orders of magnitude stronger (i.e., as for model `U11-1.0e16`), the dynamics shows a very different behavior. The amplitude

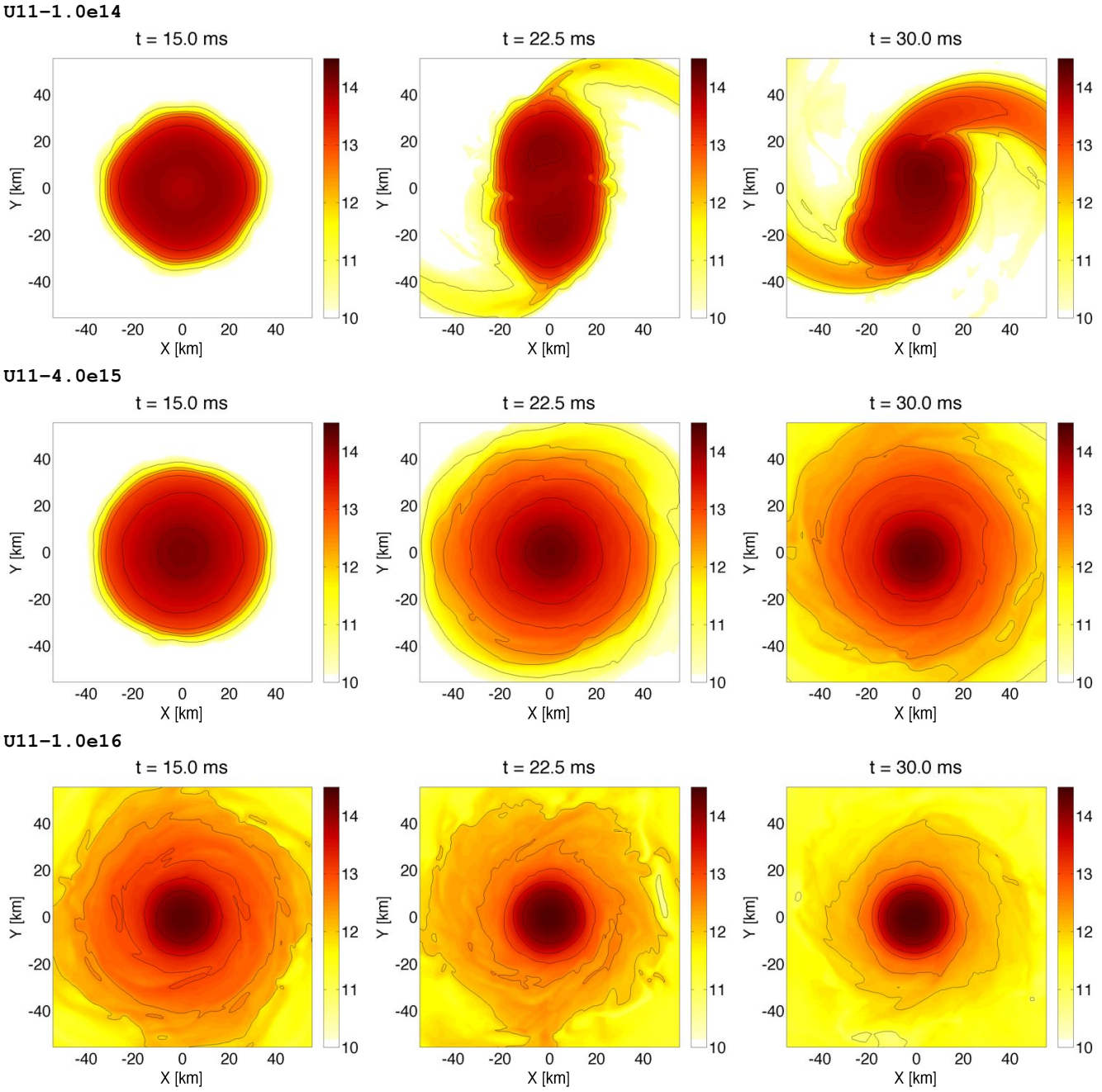

FIG. 4. Snapshots of the rest-mass density on the (x, y) plane for model `U11-1.0e14` (top row), `U11-4.0e15` (central row) and `U11-1.0e16` (bottom row) at different times during the evolution, namely, $t = 15.0$ ms (left column), $t = 22.5$ ms (central column) and $t = 30$ ms (right column). Additionally, isodensity contours are shown for $\rho = 10^{6},\ 10^{11},\ 10^{12},\ 10^{12.5},\ 10^{13},\ 10^{13.5}$, and 10^{14} g cm^{-3}.

of the oscillations in η_+ is negligible and η does not grow exponentially, being two orders of magnitude lower than it is for model `U11-1.0e14` during the whole evolution. This indicates that although the model is unstable in the absence of magnetic fields, no bar-mode deformation develops in this case over a timescale of ~ 35 ms of evolution and for this magnetic-field strength.

For intermediate initial poloidal magnetic fields, we find a significant change in the dynamics by simply varying the field strength by a factor of two, which corresponds to a change of a factor of four in the magnetic energy. Moreover, in model `U11-2.0e15` the bar-mode instability still develops, even though it takes a little longer to grow, while model `U11-4.0e15` is stable and the bar-mode instability is suppressed, since η does not show an exponential growth. As a result, we can bracket the stability threshold for the development of the bar-mode instability between these two models in the presence of strong magnetic fields (cf., Fig. 2).

To better illustrate the different behavior of the matter evolution for different initial poloidal magnetic field strengths, in Fig. 4 we show three snapshots of the evolution of the rest-mass density on the (x, y) plane for three of the above models (i.e., models `U11-1.0e14`, `U11-4.0e15` and `U11-1.0e16`) at times $t = 15.0,\ 22.5,\ 30.0$ ms. In particular, in the top row of Fig. 4 we show the evolution of model `U11-1.0e14`, which as discussed previously is bar-mode unstable as also its un-magnetized counterpart. After 15 ms we can already observe a small deformation with respect to the initial axisymmetric configuration, which is then amplified until a bar is fully formed after about 10 ms of the first oscillations observed in η_+. In the central row we show the evolution of model `U11-4.0e15`, which as mentioned before is instead stable against bar-mode deformations due to the presence of the strong magnetic field. In this case, after 15 ms the density profile has already changed, turning from an initial toroidal profile (cf., Fig. 1) to an oblate profile with its maximum residing on the z-axis. Later in the evolution, we observe an increase in the central density and the outer layers expanding well beyond the borders of the finest grid. Finally, on the bottom row we show snapshots of the density for model `U11-1.0e16`, which refers to the strongly magnetized case and which is also stable and shows a similar behavior to the previous model. The only important difference is the larger increase of the central rest-mass density and the more significant expansion of the outer layers of the star. Indeed, after the first 15 ms of evolution, matter has been shed already beyond the edges of the finest grid.

A deeper insight in the matter dynamics in the three different cases discussed above can be gained through the spacetime diagrams shown Fig. 5, and that are reminiscent of similar ones first presented in Ref. [28]. In particular, the left column of Fig. 5 shows the rest-mass density profile along the x-axis for the three models `U11` using both a colormap (see the right-edge of the different panels) and some representative contour lines; note that the colorcode and the color ranges are the same in the three cases. It is worth mentioning that the low-magnetic-field model `U11-1.0e14` (top panel in left column) shows the evolution we expect from a bar-mode unstable model, since the bar deformation is clearly visible after about 20 ms. The highly magnetized model `U11-4.0e15` (middle panel in left column), on the other hand, shows no bar deformation and exhibits instead a transition from a toroidal configuration to an oblate one as is evident in Fig. 4. In addition, a small amount of matter is shed on the equatorial plane after about 15 ms of evolution. Finally, for the very highly magnetized model `U11-1.0e16` (bottom panel in left column), the expansion of the outer layers is much more rapid and the stellar material reaches a size of about 100 km (not shown in the figure), which is almost twice as large as for model `U11-4.0e15`. The ejected material creates an extended and flattened envelope of high-density matter[1], with rest-mass densities as high as 10^{12} g cm^{-3}.

To determine whether the ejected matter is gravitationally bound or not, we look at the time component of the fluid four-velocity u_t (central column of Fig. 5) since the local condition $u_t > -1$ provides a necessary although not sufficient condition for a fluid element to be unbound [28]. We recall that this condition is exact only in an axisymmetric and stationary spacetime. These requirements are not matched during the matter-unstable phase, but the conditions can be used nevertheless as a first approximation to determine whether part of the material is actually escapes to infinity during the evolution. As is evident from Fig. 5, this condition is fulfilled throughout the whole evolution for the highly magnetized models `U11-1.0e16` and `U11-4.0e15` not only on the finest refinement level shown in Fig. 5, but on the whole computational domain. However, this is not the case for model `U11-1.0e14` at the time the bar-mode instability is fully developed. In fact, in this case we observe that a certain amount of unbound matter is shed in correspondence with the spiral arms of the bar. The ejection of matter occurs only in very low-density regions around the star, where $\rho \simeq 10^{10}$ g cm^{-3} $\simeq 10^{-4}\,\rho_c$. Overall, the total amount of matter (both bound and unbound) escaping from the outer grid after 20 ms of evolution is less than 0.2% of the total initial rest mass of the NSs.

We complete the description of the dynamics of these three `U11` models by reporting in the right column of Fig. 5 the spacetime diagram relative to the angular velocity Ω along the x-axis. We recall that all models have the maximum of the Ω at the stellar center (cf., Fig. 2) and this remains the case also for the low-magnetic-field and bar-mode unstable model `U11-1.0e14`, modulo the variations brought in by the development of the instability. On the other hand, for models `U11-4.0e15` and `U11-1.0e16`, the angular velocity at the stellar center first increases, then reaches a maximum and later decreases again; at the same time, the outer layers of the star expand and the maximum of the angular velocity occurs at larger radii. By the time an extended flattened envelope has been produced near the equatorial plane, much of the differential rotation has been washed out and the NS has acquired a central angular velocity that is smaller but mostly uniform.

We can summarize the main features described in detail above for the three magnetized `U11` models as follows:

- model `U11-1.0e14` is still bar-mode unstable and no effects are evident on the onset and development of the instability; a very small fraction of the rest-mass is shed at the edges of the bar-deformed object.

- model `U11-4.0e15` is bar-mode stable for the timescales considered here and after about 25 ms of evolution it settles into a more compact configuration; the new equilibrium structure has an almost uniform angular velocity and is surrounded by a differentially and flattened envelope.

[1] It is tempting and sometimes encountered in the literature to refer to the envelope as "disk" or "torus"; however, we find this is very misleading as the envelope is not disjoint from the star but rather an integral part of it which should not be discussed separately.

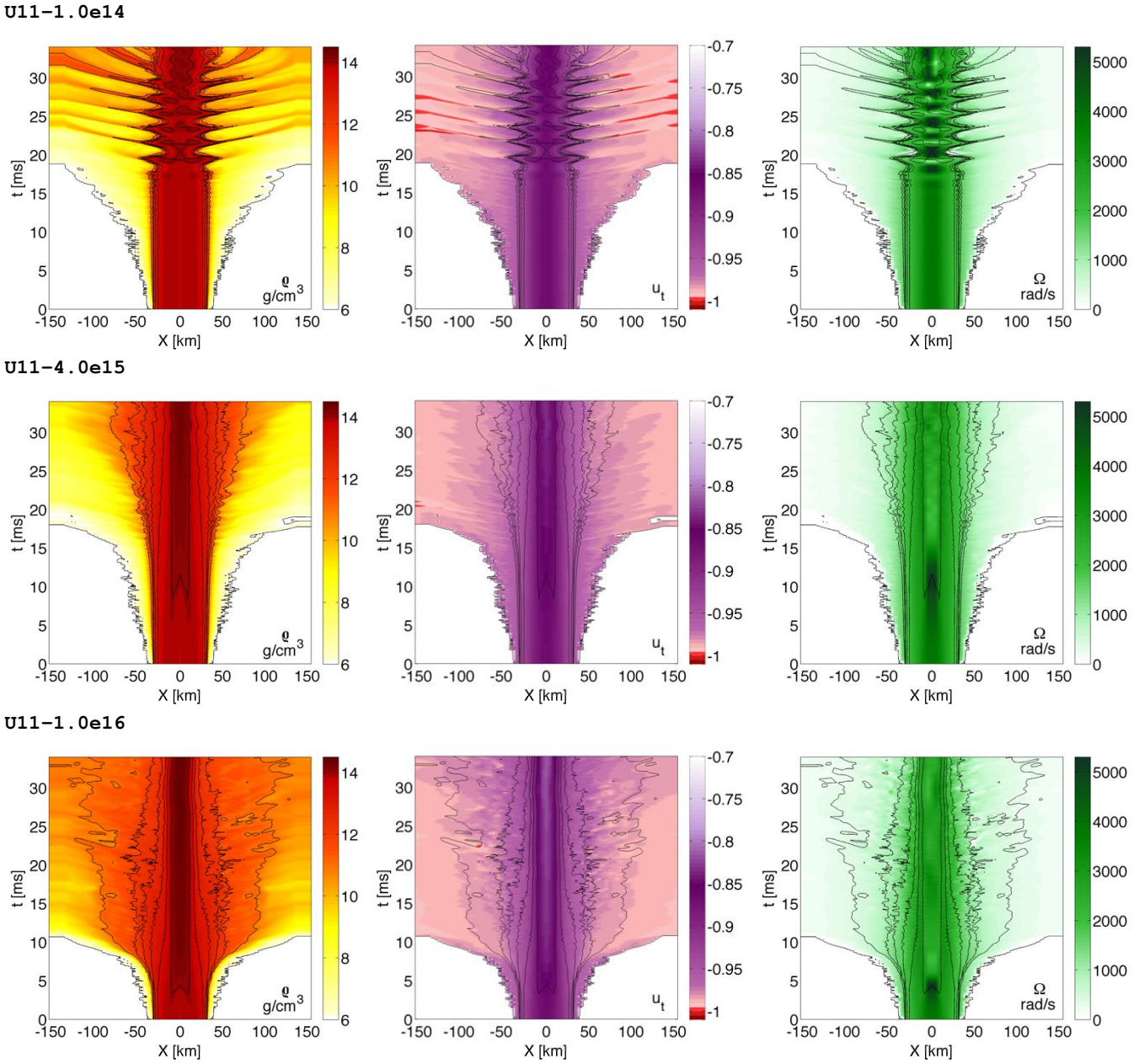

FIG. 5. Spacetime diagrams of the evolution of the rest-mass density ρ (left column), of the time-component of the fluid four-velocity u_t (central column), and of the angular velocity Ω (right column) along the x-axis. The models considered here are `U11-1.0e14` (top row), `U11-4.0e15` (central row), and `U11-1.0e16` (bottom row). The color code is indicated to the right of each plot. In addition, all diagrams also report isodensity contours of the rest-mass density $\rho = 10^6,\ 10^{11},\ 10^{12},\ 10^{12.5},\ 10^{13},\ 10^{13.5}$, and 10^{14} g cm^{-3}.

- model `U11-1.0e16` is also bar-mode stable with a dynamics that resembles that of model `U11-4.0e15`; the main differences are the shorter timescales required to reach equilibrium and the flattened envelope with larger mean rest-mass densities present in model `U11-4.0e15`.

Altogether, the behavior summarized above is consistent with what we would expect for highly magnetized and differentially rotating fluids. Under these conditions, in fact, magnetic braking transfers angular momentum from the core to the outer layers, changing the rest-mass density and the rotation profiles of the star. Because during this process part of the rotational energy of the star is tapped, the onset of the instability is inhibited.

We next discuss the dynamics of the magnetic fields, in Fig. 6, and show for comparison representative snapshots of the total electromagnetic energy density $T^{00}_{\rm em}$ (shown with a colorcode) as measure in the Eulerian frame and the magnetic field lines (shown as white solid lines), as measured on a horizontal plane at $z \simeq 1.5$ km, corresponding to the three mag-

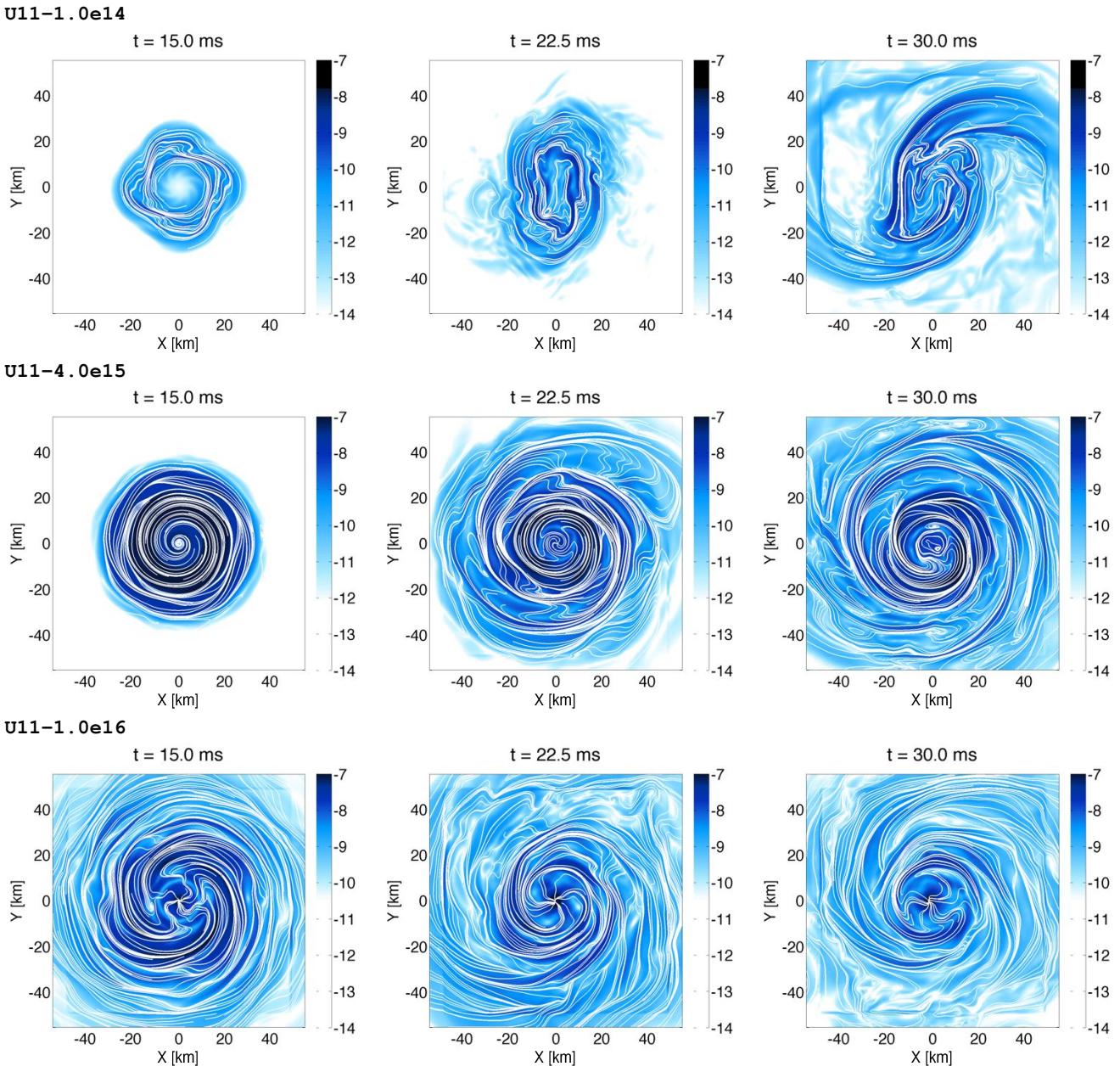

FIG. 6. Snapshots of the total electromagnetic energy density $T^{00}_{\rm em}$, as measured in the Eulerian frame, on a horizontal plane at $z \simeq 1.5$ km for model `U11-1.0e14` (top row), `U11-4.0e15` (central row), and `U11-1.0e16` (right row), at different times during the evolution, namely, $t = 15.0$ ms (left column), $t = 22.5$ ms (central column), and $t = 30$ ms (right column). The magnetic field lines are shown with white solid lines.

netized `U11` models studied before. Note that all the panels have the same color ranges but that the colormap is different at different times (i.e., in different columns) in order to better highlight the internal structure of the electromagnetic field. The various columns refer to different times and coincide with those already reported in Fig. 4.

As expected under the ideal-MHD approximation, with the magnetic field being frozen into the fluid, the field lines are dragged along with the fluid in differential rotation and rapidly wind on a timescale of very few milliseconds, leading to a sudden formation and rapid linear growth of a toroidal magnetic field component. This component is soon amplified far above the initial poloidal one. The winding of the field lines and the linear growth of the toroidal field are present in all three models and are independent of the initial poloidal magnetic field strength. The reason is that they only depend on the angular velocity profile, or equivalently on the differential rotation law, which is the same for all `U11` models in the first part of the evolution. It interesting to note in the first row of the figure (i.e., the unstable model `U11-1.0e14`), that the distortion of

the magnetic field lines also mimics the bar-mode deformation as the star undergoes the development of the instability.

A more quantitative assessment of the influence of the magnetic fields on the unstable models has been obtained after performing a number of simulations of models U3, U11 and U13, with initial poloidal magnetic fields varying between the two extreme cases presented in Figs. 4–6. More specifically, we have performed 27 simulations with initial maximum magnetic fields in the range $B^z_{\rm max}|_{t,z=0} = 1.0 \times 10^{14}$ and 1.0×10^{16} G. The results of this extensive investigation are collected in Figs. 2 and 7, as well as in Table II, which reports the measured growth time of the instability $\tau_{\rm bar}$ and its frequency $f_{\rm bar}$. In particular, Fig. 2 reports the initial models within a $(\beta,\, \beta_{\rm mag})$ diagram and allows one to easily distinguish the ranges of rotational and magnetic energies that give rise to the development of a dynamical bar-mode instability. It is, in fact, easy to distinguish models that are bar-mode stable (blue symbols) from those that are unstable (red symbols) at zero magnetizations; of course, models that are stable at zero magnetizations are also stable at all magnetizations (this is marked with the vertical red dashed line). Equally simple is to distinguish models that although unstable in the absence of magnetic fields (red squares), become stable with sufficient magnetization (red triangles). As an example, for models U3 the threshold between squares and triangles appears for initial maximum magnetic fields $B^z_{\rm max}|_{t,z=0} > 6.0 \times 10^{14}$ G, while for models U11 and U13 the threshold is at about 2.0×10^{15} and 2.4×10^{15} G respectively. As a result, only the light-red shaded area in Fig. 2 collects stellar models that are bar-mode unstable. Outside this region, either the rotational energy is insufficient, or the magnetic tension is too strong to allow for the development of the instability.

Similarly, Fig. 7 reports the measured growth time of the instability $\tau_{\rm bar}$ (and the corresponding error bars) for the three different classes of unstable models (U3, U11 and U13) as a function of the magnetization parameter $\beta_{\rm bar}$. Taking the horizontal dashed lines as references for the unmagnetized models, it is easy to realize that as the magnetization increases, so does the growth time for the instability. This behavior can be physically interpreted as due to the fact that as the magnetic field strength increases, so does the timescale over which the magnetic tension needs to be won to develop a bar deformation[2].

We can next focus on the growth of the magnetic-field strength in bar-mode unstable models as this also offers the opportunity for a number of useful considerations. More specifically, we show in Fig. 8 the evolution of the total electromagnetic energy $E_{\rm mag}$ normalized to the initial values for models U11 (left panel), U13 (middle panel) and U3 (right panel), and for different initial poloidal magnetic-field strengths. The first obvious thing to notice in Fig. 8 for all the magnetizations considered for model U11 is that the growth of the magnetic energy is linear in time initially. This is not surprising and is indeed the mere manifestation of the "frozen-in"

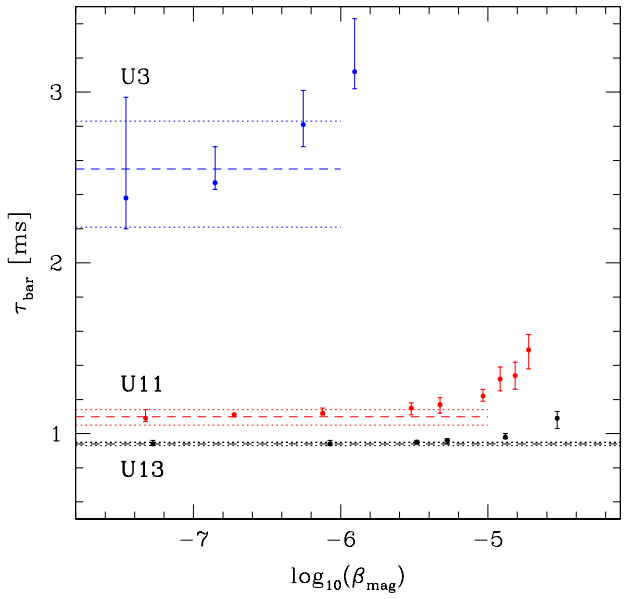

FIG. 7. Growth time of the bar-mode instability for the three unstable models U3 (blue), U11 (red) and U13 (black), shown as a function of the initial magnetization. The horizontal dashed lines report the growth times in the absence of magnetic fields, while the dotted lines represent the corresponding error bars.

condition of the magnetic field within the ideal-MHD approximation. Using the induction equation it is, in fact, straightforward to show that in a linear regime the differential rotation will generate toroidal magnetic field at a rate which is linear in time. This is because as long as the stellar configuration remains essentially axisymmetric the poloidal magnetic field is not affected by the newly produced toroidal field, and the total electromagnetic energy can only grow linearly with time tapping part of the rotational energy of the star.

As a result of this growth, the toroidal component becomes rapidly larger than the initial poloidal one and an amplification of the total electromagnetic energy takes place for all models that reaches a higher value of about two orders of magnitude over a timescale of ~ 10 ms. After this initial phase, the toroidal field keeps growing at a slower rate, reaching a saturation with the maximum amplification being almost independent of the initial poloidal magnetic field strength and of the rotation of the stellar model. The only exceptions to this behavior appear in models with ultra-strong magnetic fields, in which cases the saturation occurs at values that are about two orders of magnitude smaller (cf., blue solid lines in the different panels of Fig. 8).

Interestingly, for models U11 and U13, that is for the unstable models with small growth rates and far from the threshold of the dynamical bar-mode instability, the linear growth of the magnetic field is accompanied also by a rather short exponential growth of the magnetic field. While this behavior is very similar to the one seen in Ref. [34], where it was

[2] Note that the error bars are larger for model U3 because this is closer to the stability threshold (cf., Table I).

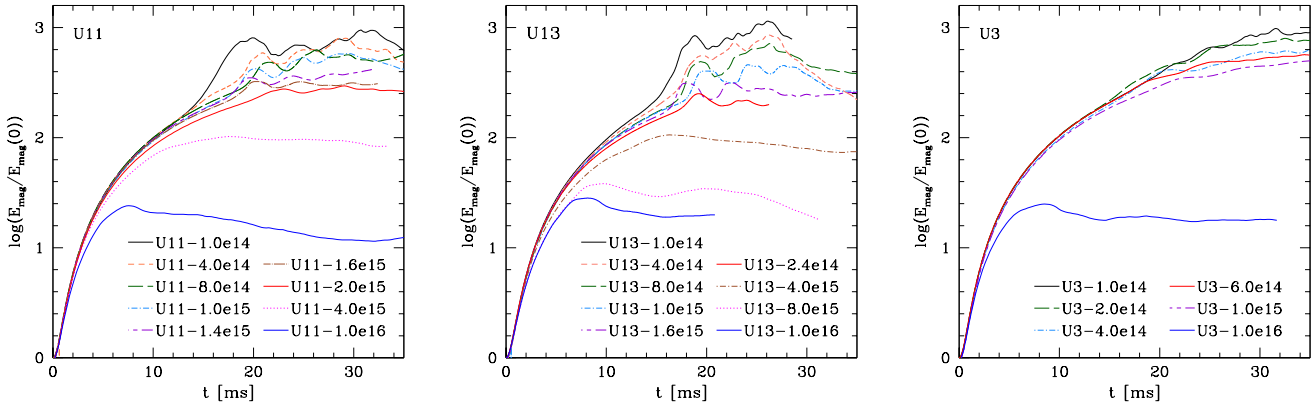

FIG. 8. *Left panel:* evolution of the total magnetic energy $E_{\rm mag}$, normalized to its initial value, for models `U11` and different values of the initial poloidal magnetic field. The black solid line refers to the less magnetized case, the blue solid line for the most magnetized case, and a red solid line for the last unstable model, before excessive magnetic tension suppresses the instability. *Middle and right panels:* the same as in the left panel, but for model `U13` and model `U3`, respectively.

Model	$\beta_{\rm mag}$	t_1 [ms]	t_2 [ms]	$\eta_{\rm max}$	$\tau_{\rm bar}$ [ms]	$f_{\rm bar}$ [Hz]
U11-0.0e00	0.0	16.2	18.3	0.784	$1.10^{+0.04}_{-0.05}$	490^{+1}_{-4}
U11-1.0e14	4.7×10^{-8}	14.7	16.8	0.787	$1.09^{+0.05}_{-0.02}$	491^{+3}_{-5}
U11-2.0e14	1.9×10^{-7}	15.0	17.0	0.778	$1.11^{+0.02}_{-0.01}$	488^{+1}_{-1}
U11-4.0e14	7.5×10^{-7}	15.1	17.7	0.773	$1.12^{+0.03}_{-0.01}$	488^{+2}_{-2}
U11-8.0e14	3.0×10^{-6}	14.8	18.2	0.754	$1.15^{+0.03}_{-0.04}$	490^{+2}_{-5}
U11-1.0e15	4.7×10^{-6}	14.2	16.8	0.751	$1.17^{+0.04}_{-0.05}$	491^{+2}_{-4}
U11-1.4e15	9.2×10^{-6}	13.9	16.2	0.714	$1.22^{+0.04}_{-0.03}$	491^{+1}_{-2}
U11-1.6e15	1.2×10^{-5}	14.5	17.3	0.681	$1.32^{+0.07}_{-0.07}$	489^{+2}_{-1}
U11-1.8e15	1.5×10^{-5}	13.2	16.7	0.639	$1.34^{+0.08}_{-0.08}$	490^{+2}_{-1}
U11-2.0e15	1.9×10^{-5}	14.8	17.3	0.532	$1.49^{+0.09}_{-0.11}$	489^{+4}_{-2}
U13-0.0e00	0.0	11.6	14.7	0.865	$0.94^{+0.01}_{-0.01}$	449^{+1}_{-3}
U13-1.0e14	5.3×10^{-8}	12.2	15.3	0.866	$0.94^{+0.02}_{-0.01}$	450^{+2}_{-2}
U13-4.0e14	8.5×10^{-7}	12.7	15.8	0.851	$0.94^{+0.02}_{-0.01}$	450^{+2}_{-2}
U13-8.0e14	3.3×10^{-6}	12.7	15.8	0.842	$0.95^{+0.01}_{-0.01}$	451^{+1}_{-2}
U13-1.0e15	5.3×10^{-6}	14.1	16.7	0.833	$0.96^{+0.01}_{-0.02}$	451^{+3}_{-1}
U13-1.6e15	1.3×10^{-5}	11.6	14.8	0.813	$0.98^{+0.02}_{-0.01}$	456^{+1}_{-2}
U13-2.4e15	3.0×10^{-5}	13.0	15.9	0.734	$1.09^{+0.04}_{-0.06}$	461^{+1}_{-1}
U3-0.0e00	0.0	24.8	26.4	0.486	$2.55^{+0.28}_{-0.34}$	540^{+2}_{-2}
U3-1.0e14	3.5×10^{-8}	24.9	27.1	0.472	$2.38^{+0.59}_{-0.18}$	537^{+5}_{-10}
U3-2.0e14	1.4×10^{-7}	26.1	28.0	0.456	$2.47^{+0.21}_{-0.04}$	536^{+5}_{-3}
U3-4.0e14	5.6×10^{-7}	24.0	26.3	0.421	$2.81^{+0.20}_{-0.13}$	537^{+2}_{-3}
U3-6.0e14	1.2×10^{-6}	24.2	25.7	0.300	$3.12^{+0.31}_{-0.10}$	535^{+5}_{-6}

TABLE II. Main properties of the initial part of the instability for model `U11`, `U13` and `U3` for different values of the initial poloidal magnetic field. Here we report the representative times t_1 and t_2 between which the maximum values of the distortion parameter η, the growth times $\tau_{\rm bar}$ and the frequencies $f_{\rm bar}$ are computed.

attributed to the development of the MRI, a similar conclusion cannot be drawn with confidence here. On the one hand, there are a number of combined elements that seem to support the suggestion that the exponential growth is the result of the development of an MRI: (i) the instability disappears with decreasing resolution (the smallest wavelength needs to be properly resolved); (ii) the growth rate does not depend on the initial poloidal magnetic field (in the simplest description the growth rate depends only on the local angular velocity); (iii) the exponential growth is followed by a rapid decay possibly caused by reconnection processes (this behavior was also found in Ref. [34]); (iv) the exponential growth disappears for sufficiently strong magnetic fields (the bar-mode deformation is no longer the lowest energy state energetically because of the large magnetic-field contribution). However, our resolutions here are considerably coarser than those employed in Ref. [34], and it is therefore difficult to see the appearance of channel-flow structures typical of the MRI and hence to make robust measurements of the wavelengths of the fastest-growing modes. One important feature of models `U11` and `U13` is that they develop pronounced bar-mode deformations (they are further away from the stability threshold in Fig. 2) and it is therefore possible that these large deviations from axisymmetry act as an additional trigger, favouring the development of the MRI[3]. This could explain why an exponential growth is seen in these models despite the coarse resolution. At the moment this is just a conjecture, which however, if confirmed, could shed light on the sufficient conditions for the development of the MRI and in particular on the degree of axisymmetry needed by the system. Additional simulations at much higher resolutions will be necessary to address this point in the future.

Interestingly, no exponential growth has been measured in the dynamics of model `U3` for all the different magnetizations considered (cf., right panel of Fig. 8). Although the angular

[3] We recall that the assumption of axisymmetry is a fundamental one in all perturbative calculations on the MRI and that it is exactly the absence of axisymmetry that allows for the development of dynamos against the limitations of the Cowling theorem [57].

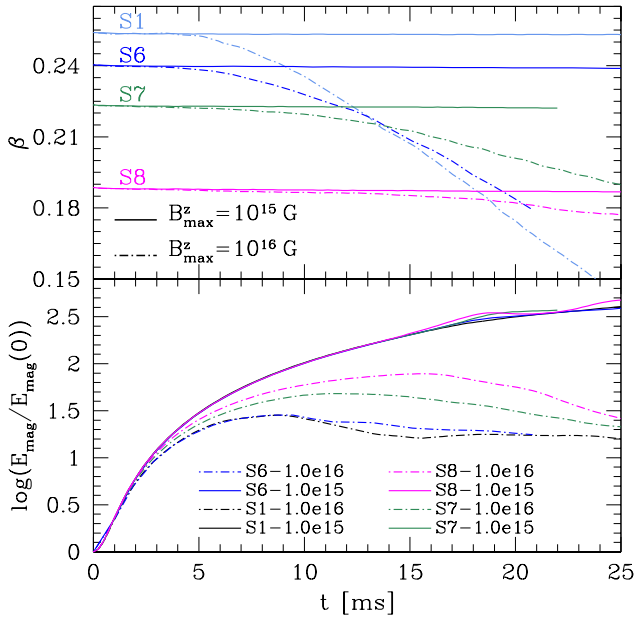

FIG. 9. Evolution of the rotation parameter $\beta := T/|W|$ (top panel) and of the total magnetic energy normalized to its initial value (bottom panel) for models `S1`, `S6`, `S7` and `S8` which are stable against the bar-mode deformation in the un-magnetized case. In both panels the solid lines refer to models with $B^z_{\rm max}|_{t,z=0} = 10^{15}$ G, while the dash-dot lines to models with $B^z_{\rm max}|_{t,z=0} = 10^{16}$ G.

frequency of these models is larger than that of `U11` and `U13` and hence the timescale for the development of the MRI $\tau_{\rm MRI}$ would be correspondingly shorter ($\tau_{\rm MRI} \sim \Omega^{-1}$). The evolutions have been carried out on sufficiently long timescales to allow for the potential appearance of the MRI. This behavior is indeed consistent with the conjecture discussed above, since this class of models is very close to the threshold for the development of the bar-mode instability. As a result, these models experience much smaller bar-mode deformations and maintain a configuration which is more axisymmetric than those found in models `U11` and `U13`. Because these conditions are more similar to those assumed by perturbative MRI analysis, the corresponding predictions are expected to be more accurate. Hence, it is not surprising that no MRI is observed in this case simply because no MRI can be seen for these quasi-axisymmetric objects at these resolutions.

B. Effects of the magnetic field on stable models

After having discussed in detail the properties of the dynamics of bar-mode *unstable* models, we now turn to illustrating how magnetic fields affect the dynamics of bar-mode *stable* models. Although these are comparatively simpler configurations, they provide a number of interesting considerations, as we will see.

We recall that using the same EOS adopted here, Ref. [10] has determined the threshold for the development of a dynamical bar-mode instability to be $\beta \simeq 0.255$ (cf., Fig. 2). We have therefore considered a number of stable models, namely `S1`, `S6`, `S7` and `S8`, that are increasingly more distant from the threshold. For each of these classes we have then added two different magnetic-field strengths, namely, $B^z_{\rm max}|_{t,z=0} = 1.0 \times 10^{15}$ G and $B^z_{\rm max}|_{t,z=0} = 1.0 \times 10^{16}$ G, and performed simulations to record the different impact of the magnetic fields on the dynamics.

Of course, since these models are already stable in the absence of magnetic fields, they will remain stable also with the additional magnetic tension. However, while models with $B^z_{\rm max}|_{t,z=0} = 1.0 \times 10^{15}$ G do not show in their dynamics any significant deviation from a purely hydrodynamical evolution, models with $B^z_{\rm max}|_{t,z=0} = 1.0 \times 10^{16}$ G do quite the opposite. This is shown in the top panel of Fig. 9, which reports the evolution of the rotation parameter β for all these stable models. Solid lines of different color refer to the different models but all having an initial magnetic field $B^z_{\rm max}|_{t,z=0} = 1.0 \times 10^{15}$ G. On the other hand, dot-dashed lines of different color refer to models with $B^z_{\rm max}|_{t,z=0} = 1.0 \times 10^{16}$ G. Note that for comparatively "low" magnetic fields, the rotation parameter does not show any significant variation from the initial value over a timescale of around 25 ms, with changes that are $\lesssim 0.4\%$ for model `S1` and $\lesssim 1.0\%$ for model `S8`. On the other hand, for magnetic fields that are one order of magnitude larger, the rotation parameter changes significantly, decaying almost linearly with time. This is obviously due to the combined action of the differential rotation and of the magnetic winding, which increases the magnetic tension and drives the NS towards a configuration that is uniformly rotating. This is also very clearly shown in the bottom panel of Fig. 9, which reports the evolution of the normalized magnetic energy. It is then rather clear that while the energy increases (linearly) with time in the case of comparatively small magnetic fields (solid lines), it stops growing and saturates in the case of large magnetic fields (dot-dashed lines). Over the timescale of the simulations, ~ 25 ms, the magnetic energy has increased of almost three orders of magnitude in the former case and of only one in the latter case.

We can use the results in the top panel of Fig. 9 to obtain an important estimate on the rate at which the stellar rotational energy is completely tapped by the generation of a toroidal magnetic field. In particular, using the numerical data it is possible to express β as

$$\beta(t) \simeq \beta_0 + a \exp\left(1 - \frac{b}{t}\right) - ct\,, \qquad (4.1)$$

where $\beta_0 := \beta(t = 0)$ and a, b, c are three constant coefficients to be computed from a fit to the numerical data. Using this expression is possible to compute the "braking timescale" $\tau_{\rm br}$, that is, the timescale needed for an axisymmetric and differentially rotating configuration to lose all of its rotational energy via magnetic-field shearing and thus be brought to have $\beta(\tau_{\rm br}) = 0$[4]. The numerical fits show that the parameter b we

[4] It is perfectly plausible that a nonrotating configuration is never reached

obtain is of the order of the simulation time and indeed the expression in Eq. (4.1) is used only for time $t < b$. Considering the limit $t \gg b$ in the expression above and after a little bit of algebra we can show that the timescale is

$$\tau_{\rm br} \simeq \frac{\beta_0 + ae}{c} \,. \tag{4.2}$$

Interestingly, for the EOS and the magnetic field of 10^{16} G considered here, the coefficients a and c have a simple dependence on β_0[5], i.e.,

$$a \simeq k_1 + k_2 \beta_0 \,, \qquad\qquad c \simeq k_3 + k_4 \beta_0 \,, \tag{4.3}$$

where $k_1 \simeq -0.0589$, $k_2 \simeq 0.332$, $k_3 \simeq -0.017$ ms^{-1} and $k_4 \simeq 0.092$ ms^{-1}. As a result, the general expression for the braking time is now just a function of the initial rotation parameter

$$\tau_{\rm br} \simeq \frac{[\beta_0 + e\ (k_1 + k_2 \beta_0)]}{k_3 + k_4 \beta_0} \,, \tag{4.4}$$

and of the four coefficients k_1, k_2, k_3 and k_4. As an example, we can use the expression (4.4) to estimate the braking time for models `S1` and `S8`, readily obtaining $\tau_{\rm br} \sim 0.050$ s and $\tau_{\rm br} \sim 0.56$ s, respectively.

Much of what is discussed above can also be deduced when analyzing the structural changes in the NSs. These are shown in Fig. 10, where we report the initial (i.e., at $t = 0$ ms with black lines) and the final (i.e., at $t = 25$ ms with blue lines) normalized profiles along the x-direction of the angular velocity (solid lines; cf., left y-axis of the figure) and of the rest-mass density (dashed lines; cf., right y-axis of the figure) for model `S1` and the two different values of the magnetic field ($B^z_{\rm max}|_{t,z=0} = 1.0 \times 10^{15}$ G in the top panel and $B^z_{\rm max}|_{t,z=0} = 1.0 \times 10^{16}$ G in the bottom one).

Modulo of course the fact that the star will have shed some matter and produced a more extended, very low-density outer mantle, it is clear from the top panel of Fig. 10 that the angular velocity and rest-mass density in the stellar core hardly change. This is to be contrasted with what shown in the bottom panel, which clearly shows a very large increase of the rest-mass density in the inner regions of the star and a corresponding decrease in the outer ones. At the same time, the angular velocity profile has flattened considerably and indeed the star is essentially axisymmetric and in uniform rotation within a coordinate radius of $\simeq 15$ km.

As a final remark, we note that the considerations made here and in particular the braking timescale estimated in Eq. (4.2), are of course of more general validity than the bar-mode instability context considered here. Compact, axisymmetric and differentially rotating magnetized configurations

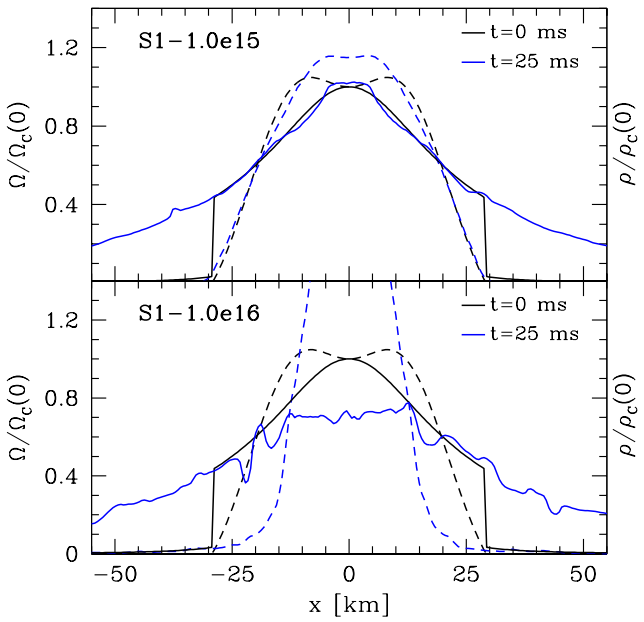

FIG. 10. Initial (i.e., shown with black lines at $t = 0$ ms) and the final (i.e., shown with blue lines at $t = 25$ ms) normalized profiles along the x-direction of the angular velocity (solid lines) and of the rest-mass density (dashed lines) for model `S1` and the two different values of the magnetic field, i.e., 10^{15} G (top panel) and 10^{16} G (bottom panel).

can in fact be produced in a number of scenarios, from stellar-core collapse to the merger of binary NSs. Determining the timescales over which uniform rotation is established under controlled setups in terms of differential-rotation laws and magnetizations is of course of great importance and will be addressed in a future work.

V. CONCLUSIONS

We have presented a study of the dynamical bar-mode instability in differentially rotating and magnetized NSs in full general relativity and investigated how the presence of magnetic fields affects the onset and the development of the instability. In order to do that, we have performed 3D ideal-MHD simulations of a large number of stellar models that were already studied in the absence of magnetic fields [10, 11, 36], by adding an initial purely poloidal magnetic field with strengths between 10^{14} and 10^{16} G. In this way, we were able to explore quite extensively the parameter space (β, $\beta_{\rm mag}$) from $\beta = 0.1886$ to 0.2812, determining a threshold for the onset of the instability both in terms of the rotation parameter $\beta = T/|W|$ and of the magnetization parameter $\beta_{\rm mag} = E_{\rm mag}/(T + |W|)$. In all cases considered, the differential rotation shears the poloidal magnetic field, generating a toroidal component that grows linearly in time, and which soon provides the largest contribution to the total electromagnetic en-

because the system will first collapse to a black hole. Of course this is possible only for initial stellar configurations that are supermassive (see [58] for the exploration of this possibility).

[5] The coefficient b describes the transient and is not relevant to study the asymptotic solution.

ergy.

When considering initial stellar models that are bar-mode unstable in the absence of magnetic fields, we found that no effects are present on the dynamics of the bar-mode deformation for initial poloidal magnetic fields that are $\lesssim 10^{15}$ G, with the exact threshold depending on the rotational properties of the initial model and being higher for slower rotating models. This is not particularly surprising given that in these cases the magnetic energy, even the one produced via magnetic-field shearing, is only a small contribution to the total energy of the system. For initial magnetic fields that are instead $\gtrsim 10^{16}$ G or larger, the corrections introduced by the magnetic tension become quite large. In particular, below a critical $\beta_{\rm mag}$, the development of the instability is modified, showing growth rates and bar-mode distortions that become smaller with increasing magnetic fields, and possibly exhibiting an exponential growth of the toroidal component at later times. Above a critical $\beta_{\rm mag}$, on the other hand, the instability is totally suppressed as the enormous magnetic tension cannot be overcome by the differential rotation. Under these conditions, the star sheds its outer layers leading to an extended, axisymmetric object with a high, uniform-density core and a low-density, slowly rotating envelope.

On the basis of the phenomenology discussed above, and after carrying-out a large number of simulations, we were able to locate in the (β, $\beta_{\rm mag}$) diagram the regions in which the values of the rotational and magnetic energies are sufficient to give rise to the development a dynamical bar-mode instability. In this sense, our study confirms the Newtonian results of [20] and extends them to a general-relativistic framework and to a more generic range of initial conditions.

We have complemented our investigation by considering also initial stellar models that are bar-mode stable in the absence of magnetic fields. While these are comparatively simpler configurations, also in this case the magnetic fields can provide structural changes if sufficiently strong. More specifically, for magnetic fields $\gtrsim 10^{16}$ G, the stellar models are braked considerably in their rotation and evolve into configurations that have uniformly rotating extended cores with large rest-mass densities when compared to the initial values. A simple algebraic expression has been derived to estimate the timescale over which an axisymmetric and differentially rotating configuration will lose all of its rotational energy via magnetic-field shearing.

As a final remark we note that although we have restricted our attention to a simplified EOS, our results also point out that it is unlikely that very highly magnetized NSs can develop the dynamical bar-mode instability and hence be considered as strong sources of GWs.

ACKNOWLEDGMENTS

We have benefited from discussions with several colleagues and friends and we are particularly grateful to Alessandra Feo, Sebastiano Bernuzzi, Niccoló Bucciantini, Riccardo Ciolfi, Luca Del Zanna, Filippo Galeazzi, and Frank Löffler. This work has been partially supported by the "CompStar", a Research Networking Programme of the European Science Foundation and the DFG grant SFB/Transregio 7. The calculations have been performed using the HPC resources of the INFN "Theophys" cluster, the PRACE allocation (6th-call) "3dMagRoI" on CINECA's supercomputer "Fermi", the cluster 'at the Albert-Einstein Institute, and the PRACE allocation "pr32pi" on "SuperMUC" at the "Leibniz-Rechenzentrum".

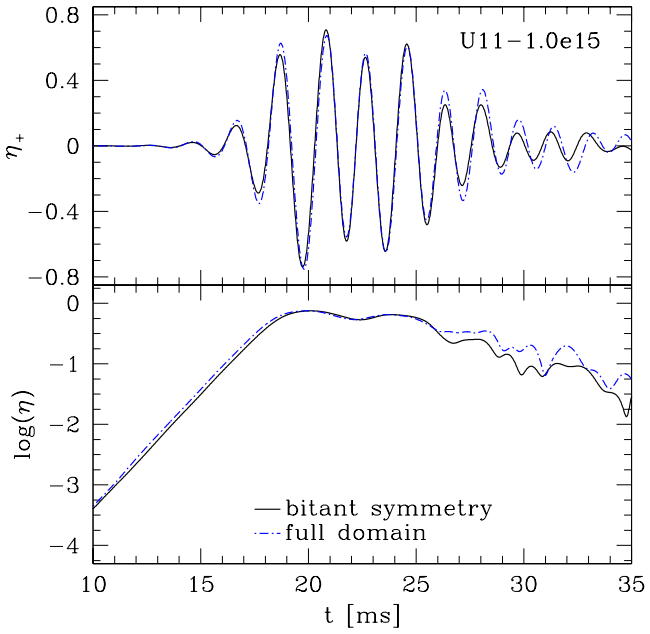

FIG. 11. Evolution of the distortion parameters η_+ (top panel) and η (bottom panel) for model `U11-1.0e15` when imposing a bitant symmetry (black solid line) or when using the full domain (blue dashed line).

Appendix A: The role of symmetries

As discussed in Sect. II, all of the results presented here were achieved with a spatial resolution $\Delta x = 0.375\, M_\odot \simeq 0.550$ km on the finest grid and exploiting a "bitant symmetry", i.e., a reflection symmetry with respect to the (x, y) plane. While this choice obviously reduces the computational costs by a factor two, it is important to verify that it does not introduce systematic effects and that all the results would be unchanged if this symmetry was suppressed.

Although the `WhyskyMHD` code employed here has been tested in a number of different scenarios and its accuracy has already been explicitly reported in various works [24, 38, 39]; nevertheless, we have performed additional tests to check that the specific settings used are sufficient to capture the main properties of the evolved systems. To this scope we have evolved the bar-mode unstable model `U11` when threaded by an initially moderate magnetic field, i.e., model `U11-1.0e15`, both when imposing the bitant symmetry and when evolving the equations in the full domain. Further-

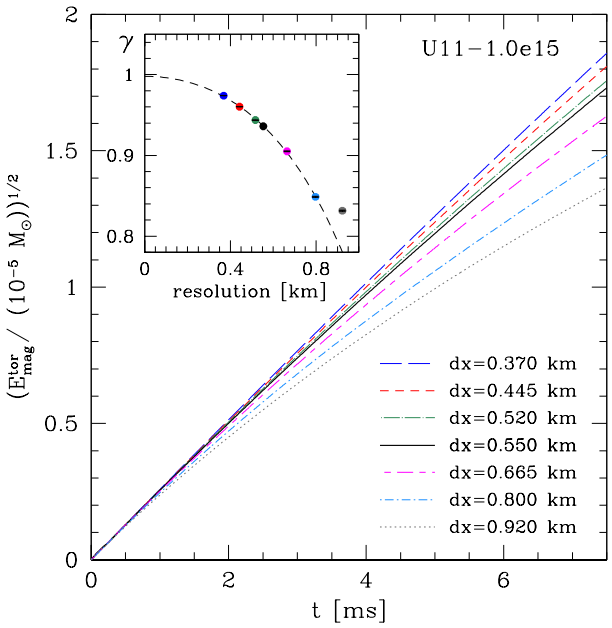

FIG. 12. Initial growth of the square root of the toroidal component of the magnetic energy $E_{\rm mag}^{\rm tor}$ [Eq. (3.13)] for different resolutions of the finest grid. The reference resolution, $\Delta x =\simeq 0.550$ km, is shown with a black solid line. The inset shows instead the growth rate γ as a function of the resolution and its fit with a quadratic function (dashed line). Note that the expected value $\gamma = 1$ is approached in the limit of $\Delta x \to 0$.

more, we have varied the resolution of more than a factor of two, that is, with the finest grid having resolutions between $\Delta x = 0.370$ km and 0.920 km.

For all these runs we computed the growth rate, $\tau_{\rm bar}$, and the frequency, $f_{\rm bar}$, of the bar-mode instability. The results of this extensive series of tests are reported in Table III) and show that these quantities do not depend on resolution within the accuracy of our estimate. Hence, we conclude that all of the results have been achieved at sufficient resolution to extract physically significant information.

In addition, we have also verified that no systematic effects have been introduced by the use of a bitant symmetry and this is shown in Fig. 11, where we report the evolution of the distortion parameters η_+ (top panel) and η (bottom panel) for model `U11-1.0e15`. The simulations have been performed at the reference resolution of $\Delta x = 0.550$ km on the finest grid, and the figure offers a comparison between a simulation using the bitant symmetry (blue dot-dashed line) and one using the full domain (black solid line). Clearly, no significant differences can be observed between the two simulations during the first 25 ms of evolution. The same conclusion holds for all quantities related to the magnetic field and they have been also monitored.

Δx $[M_\odot]$	Δx [km]	symmetry symmetry	$\eta_{\rm max}$	$\tau_{\rm bar}$ [ms]	$f_{\rm bar}$ [Hz]
0.250	0.370	bitant	0.743	$1.15^{+0.01}_{-0.01}$	491^{+1}_{-1}
0.350	0.445	bitant	0.746	$1.16^{+0.03}_{-0.03}$	492^{+1}_{-1}
0.375	0.520	bitant	0.751	$1.17^{+0.04}_{-0.05}$	491^{+2}_{-4}
0.375	0.520	full	0.753	$1.14^{+0.01}_{-0.01}$	490^{+3}_{-2}
0.450	0.665	bitant	0.745	$1.18^{+0.03}_{-0.05}$	489^{+2}_{-2}
0.540	0.800	bitant	0.754	$1.19^{+0.05}_{-0.05}$	487^{+3}_{-5}
0.625	0.920	bitant	0.743	$1.20^{+0.11}_{-0.05}$	484^{+2}_{-7}

TABLE III. Main properties of the bar-mode instability for model `U11-1.0e15` at different resolutions. Here we report the resolution in terms of solar masses and kilometers, the symmetry we imposed to the computational domain, the maximum value of the distortion parameter η, the growth times $\tau_{\rm bar}$ and the frequencies $f_{\rm bar}$ of the bar-mode deformation.

Appendix B: The role of resolution and convergence

Determining the convergence properties of our simulations is of course an essential validation of the results presented and a considerable effort has been put into performing these measures within the numerical setup used here. Lacking an analytic solution that describes the fully nonlinear development of the bar, we can only perform self-convergence tests at this stage. The results will be discussed below.

However, there is a regime in our calculations in which we can exploit the knowledge of an analytic solution and this refers to the initial shearing of the poloidal magnetic field by the differentially rotating star. It is in fact not difficult to show that within an ideal-MHD framework the induction equation predicts a growth of the toroidal magnetic field which is linear in time (see, for instance, [59] for a pedagogic presentation of the perturbed induction equation). To explore this regime we have performed a large number of simulations of model `U11-1.0e15` with varying resolution and monitored the growth of the square root of the toroidal magnetic energy $E_{\rm mag}^{\rm tor}$ [cf., Eq. (3.13]; we recall that the poloidal magnetic field is not expected to grow during this stage (cf., Sect. IV A).

Figure 12 reports the results of these simulations relatively to the first ~ 7 ms, with different curves referring to different resolutions. It is then evident that the curves are getting closer and closer to straight lines as the resolution increases. To measure whether a linear-in-time-growth is actually reached we have actually computed the growth rate "γ" by fitting the square root of the magnetic energy with a trial function which is a power-law in time with undetermined growth rate, i.e., with

$$\sqrt{E_{\rm mag}^{\rm tor}(t)} = y(t) = y_0 + m\, t^{\gamma}\,, \qquad \text{(B1)}$$

where the time interval has been selected to be between 0.2 to 5 ms.

Also reported in the inset of Fig. 12 are the values of γ (colored symbols) as a function of the resolution Δx, as well as a fit for $\gamma(\Delta x)$ (dashed line) when assuming a second-order convergence with resolution, i.e., assuming $\gamma(\Delta x) = \gamma|_{\Delta x=0} + k\,\Delta x^2$ (the point for $\Delta x = 0.920$ km has been ex-

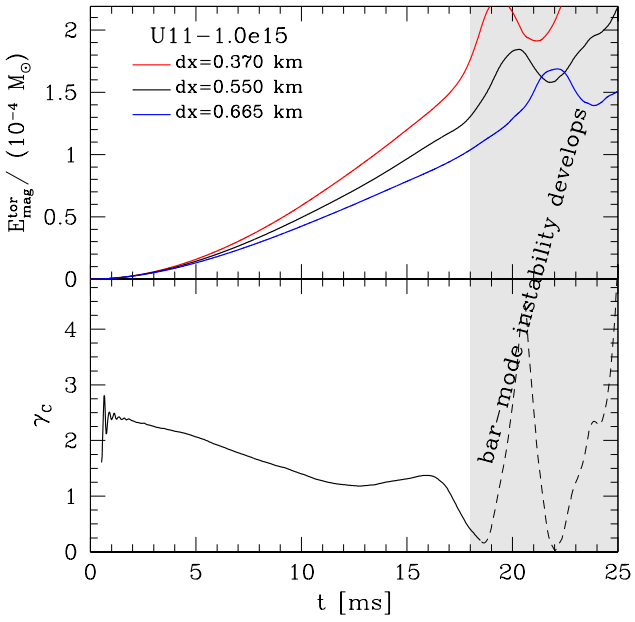

FIG. 13. *Top panel:* evolution of the toroidal component of the magnetic energy $E^{\rm tor}_{\rm mag}$ for three different resolutions. *Top panel:* order of the self-convergence test, γ_c, shown as a function of time. Note that a convergence order around 2 is measured before the bar-mode instability develops and shocks are produced (gray-shaded area).

cluded from the fit). Having made this assumption, we do find that the growth rate is in very good agreement with the one expected in this linear regime, with $\gamma|_{\Delta x=0} = 1 \pm 0.005$. Of course this result does not prove directly that we have second-order convergence over this period of time. However, what it does prove is that if a second-order convergence is assumed, then our solution matches the expected perturbative one.

Next we consider a more general calculation of the convergence order by performing again simulations of model `U11-1.0e15` for a range of resolutions. This time our results for the convergence are obtained by taking into account the data corresponding to the whole timescale of the simulations, i.e., ~ 25 ms. Also in this case we monitor the growth of the toroidal magnetic energy $E^{\rm tor}_{\rm mag}$ and report in the top panel of Fig. 13 its evolution for three runs at resolutions: $\Delta x = 0.370,\ 0.550$, and 0.665 km, respectively. The bottom panel of the same figure reports instead the convergence order γ_c, computed via a self-convergence test [48], when shown as a function of time.

In this case it is then possible to recognize that the code does indeed converge at around second order during the linear growth stage (i.e., for $t \lesssim 5$ ms), in agreement with the results found in purely hydrodynamical simulations [60], or with the new resistive code [37]. However, as the bar-mode instability develops, the second-order convergence is lost and the convergence order reduces to one. This is not surprising as the development of the bar also leads to the formation of shocks, which necessarily degrade our solution to a first-order convergence. We also note that the large variations in the convergence order shown in the gray-shaded area of Fig. 13 (i.e., for $t \gtrsim 18$ ms) are simply the consequence of the fact that the instability starts growing at different times for different resolutions and this inevitably leads to large excursions in γ_c. Because all the major considerations made about the onset and development of the bar deformation, as well as the estimates for the growth rates and frequencies, are obtained after looking at the first 20 ms of the evolution, we conclude that all of our results have been achieved with solutions converging at the expected rates.

[1] S. E. Woosley, A. Heger, and T. A. Weaver, Rev. Mod. Phys. **74**, 1015 (2002).
[2] A. Heger, C. L. Fryer, S. E. Woosley, N. Langer, and D. H. Hartmann, Astrophys. J. **591**, 288 (2003).
[3] Y. T. Liu and L. Lindblom, Mon. Not. R. Astron. Soc. **324**, 1063 (2001).
[4] C. Fryer, W. Benz, M. Herant, and S. A. Colgate, Astrophys. J. **516**, 892 (1999).
[5] N. Stergioulas, Living Rev. Relativ. **6**, 3 (2003).
[6] N. Andersson, Classical Quantum Gravity **20**, 105 (2003).
[7] S. Chandrasekhar, *Ellipsoidal Figures of Equilibrium* (Yale Univ. Press, New Haven, 1969).
[8] A. L. Watts, N. Andersson, and D. I. Jones, Astrophys. J. **618**, L37 (2005).
[9] M. Shibata, T. W. Baumgarte, and S. L. Shapiro, Astrophys. J. **542**, 453 (2000).
[10] L. Baiotti, R. De Pietri, G. M. Manca, and L. Rezzolla, Phys. Rev. D. **75**, 044023 (2007).
[11] G. M. Manca, L. Baiotti, R. D. Pietri, and L. Rezzolla, Classical Quantum Gravity **24**, S171 (2007).
[12] G. Corvino, L. Rezzolla, S. Bernuzzi, R. De Pietri, and B. Giacomazzo, Classical Quantum Gravity **27**, 114104 (2010).
[13] M. Saijo and Y. Kojima, Phys. Rev. D **77**, 063002 (2008).
[14] C. Thompson and R. C. Duncan, Astrophys. J. **408**, 194 (1993).
[15] A. Bonanno, L. Rezzolla, and V. Urpin, Astron. Astrophys. **410**, L33 (2003).
[16] P. D. Lasky, B. Zink, K. D. Kokkotas, and K. Glampedakis, Astrophys. J. **735**, L20 (2011).
[17] R. Ciolfi, S. K. Lander, G. M. Manca, and L. Rezzolla, Astrophys. J. **736**, L6 (2011).
[18] R. Ciolfi and L. Rezzolla, Astrophys. J. **760**, 1 (2012).
[19] P. D. Lasky, B. Zink, and K. D. Kokkotas, arXiv:1203.3590 (2012).
[20] K. D. Camarda, P. Anninos, P. C. Fragile, and J. A. Font, Astrophys. J. **707**, 1610 (2009).
[21] B. Paczynski, Astrophys. J. Lett. **308**, L43 (1986).
[22] D. Eichler, M. Livio, T. Piran, and D. N. Schramm, Nature **340**, 126 (1989).
[23] R. Narayan, B. Paczynski, and T. Piran, Astrophys. J. **395**, L83 (1992).
[24] L. Rezzolla, B. Giacomazzo, L. Baiotti, J. Granot, C. Kouveliotou, and M. A. Aloy, Astrophys. J. **732**, L6 (2011).
[25] E. Nakar, Phys. Rep. **442**, 166 (2007).
[26] W. H. Lee and E. Ramirez-Ruiz, New J. Phys. **9**, 17 (2007).

[27] L. Baiotti, B. Giacomazzo, and L. Rezzolla, Phys. Rev. D **78**, 084033 (2008).

[28] L. Rezzolla, L. Baiotti, B. Giacomazzo, D. Link, and J. A. Font, Classical Quantum Gravity **27**, 114105 (2010).

[29] N. Bucciantini, B. D. Metzger, T. A. Thompson, and E. Quataert, Mon. Not. R. Astron. Soc. **419**, 1537 (2012).

[30] B. Zhang, Astrophys. J. **763**, L22 (2013).

[31] M. Shibata, Y. Suwa, K. Kiuchi, and K. Ioka, Astrophys. J.l **734**, L36 (2011).

[32] K. Kiuchi, K. Kyutoku, and M. Shibata, Phys. Rev. D **86**, 064008 (2012).

[33] M. D. Duez, Y. T. Liu, S. L. Shapiro, M. Shibata, and B. C. Stephens, Phys. Rev. D **73**, 104015 (2006).

[34] D. M. Siegel, R. Ciolfi, A. I. Harte, and L. Rezzolla, Phys. Rev. D R **87**, 121302 (2013).

[35] V. Velikhov, Sov. Phys. JETP **36**, 995 (1959).
S. Chandrasekhar, Proc. Natl. Acad. Sci. **46**, 253 (1960).

[36] R. De Pietri, L. Baiotti, G. M. Manca, and L. Rezzolla, in *XXVIII Spanish Relativity Meeting (ERE 2005)*, edited by L. Mornas and J. D. Alonso (AIP Conference Proceedings, Oviedo, 2007), vol. 841, ISBN 0-7354-0333-3.

[37] K. Dionysopoulou, D. Alic, C. Palenzuela, L. Rezzolla, and B. Giacomazzo, arXiv:1208.3487, in press (2013).

[38] B. Giacomazzo and L. Rezzolla, Classical Quantum Gravity **24**, S235 (2007).

[39] B. Giacomazzo, L. Rezzolla, and L. Baiotti, Phys. Rev. D **83**, 044014 (2011).

[40] E. Schnetter, S. H. Hawley, and I. Hawke (2003).

[41] E. Schnetter, CARPET: A Mesh Refinement driver for CACTUS, URL `http://www.carpetcode.org`.

[42] L. Baiotti, I. Hawke, P. J. Montero, F. Löffler, L. Rezzolla, N. Stergioulas, J. A. Font, and E. Seidel, Phys. Rev. D **71**, 024035 (2005).

[43] P. Colella and P. R. Woodward, Journal of Computational Physics **54**, 174 (1984), ISSN 0021-9991.

[44] A. Harten, P. D. Lax, and B. van Leer, SIAM Rev. **25**, 35 (1983).

[45] Z. B. Etienne, V. Paschalidis, Y. T. Liu, and S. L. Shapiro, Phys. Rev. D **85**, 024013 (2012).

[46] H. O. Kreiss and J. Oliger, *Methods for the approximate solution of time dependent problems* (GARP publication series No. 10, Geneva, 1973).

[47] D. Pollney, C. Reisswig, L. Rezzolla, B. Szilágyi, M. Ansorg, B. Deris, P. Diener, E. N. Dorband, M. Koppitz, A. Nagar, et al., Phys. Rev. D **76**, 124002 (2007).

[48] L. Rezzolla and O. Zanotti, *Relativistic Hydrodynamics* (Oxford University Press, Oxford UK, 2013).

[49] F. Galeazzi, W. Kastaun, L. Rezzolla, and J. A. Font, arXiv:1306.4953 (2013).

[50] N. Stergioulas and J. L. Friedman, Astrophys. J. **444**, 306 (1995).

[51] H. Komatsu, Y. Eriguchi, and I. Hachisu, Mon. Not. R. Astron. Soc. **237**, 355 (1989).

[52] J. L. Friedman and N. Stergioulas, *Relativistic Rotating Stars* (Cambridge, UK: Cambridge University Press, 2012).

[53] N. Stergioulas, Living Rev. Relativ. **1**, 8 (1998).

[54] B. Giacomazzo, L. Rezzolla, and N. Stergioulas, Phys. Rev. D **84**, 024022 (2011).

[55] M. Saijo, M. Shibata, T. W. Baumgarte, and S. L. Shapiro, Astrophys. J. **548**, 919 (2001).

[56] L. Baiotti, I. Hawke, and L. Rezzolla, Classical Quantum Gravity **24**, S187 (2007).

[57] A. R. Choudhuri, *The physics of fluids and plasmas : an introduction for astrophysicists /* (1998).

[58] H. Falcke and L. Rezzolla, arXiv:1307.1409 (2013).

[59] L. Rezzolla, F. K. Lamb, and S. L. Shapiro, Astrophys. J. **531**, L139 (2000).

[60] L. Baiotti, B. Giacomazzo, and L. Rezzolla, Class. Quantum Grav. **26**, 114005 (2009).